Materials Today Bio 16 (2022) 100393

Contents lists available at ScienceDirect

Materials Today Bio

journal homepage: www.journals.elsevier.com/materials-today-bio

Two-dimensional silicene photodynamic tumor-targeting nanomedicine

Huican Duan [a], Meiqi Chang [d,**], Han Lin [e], Hui Huang [c], Wei Feng [c], Weitao Guo [a], Lina Wu [a], Yu Chen [c,*], Ruifang Zhang [b,***]

[a] Department of Ultrasound, The First Affiliated Hospital of Zhengzhou University, Zhengzhou, 450052, PR China
[b] Department of Cardiology, The First Affiliated Hospital of Zhengzhou University, Zhengzhou, 450052, PR China
[c] Materdicine Lab, School of Life Sciences, Shanghai University, 200444, PR China
[d] Central Laboratory of Shanghai Municipal Hospital of Traditional Chinese Medicine, Shanghai University of Traditional Chinese Medicine, Shanghai, 200071, PR China
[e] State Key Laboratory of High Performance Ceramics and Superfine Microstructure, Shanghai Institute of Ceramics, Chinese Academy of Sciences, Shanghai, 200050, PR China

ARTICLE INFO

Keywords:
Silicene
Two-dimensional
Nanomedicine
Photodynamic therapy
Nanobiotechnology

ABSTRACT

Since the innovative development of photosensitizers (PSs) is pivotal prerequisite for the successful clinical translation of photodynamic therapy (PDT), the unresolved challenges of classical PSs such as photobleaching, poor bioavailability, lack of tumor selectivity encourage the exploitation of new-generation PSs. In this work, we develop silicene nanosheets with unparalleled physiochemical nature and intriguing biocompatibility as the distinct two-dimensional (2D) nanoscale photosensitizer based on the mechanism of wet-chemical synthetic approach to achieve effective PDT-based tumor nanotherapy. The generation capacities of singlet oxygen ($^1O_2$) in different atmospheres have been systematically explored in depth. Furthermore, the conjunction of c (RGDyC) onto 2D silicene nanosheets (denoted as SRGD) endows the SRGD nanomedicines with specific targeting properties to $\alpha_v\beta_3$ integrin-overexpressed cancer cells, accomplishing *in vivo and in vitro* potent tumor growth inhibition efficiency. More notably, the excellent light absorption capacity of 2D silicene enables the tumor-specific photoacoustic imaging for potentiating the therapeutic guidance and monitoring. This paradigm can inspire the future design and applications of 2D silicene-based cancer-theranostic nanoplatform in biology and medicine.

1. Introduction

Cancer is deemed to the leading cause of decreasing life expectancy in the 21st century and its incidence and mortality remain rapidly growing worldwide [1]. Although the cancer-therapeutic strategies, such as chemotherapy, radiotherapy, surgery, immunotherapy and synergistic therapy are widely practiced in clinical application, the relevant systemic side effects, drug/radio resistance and high recurrence rate stimulate extensive investigations to refine the traditional cancer-treatment methods and explore the alternate therapeutic modalities [2–4]. Photodynamic therapy (PDT), emerging as a promising strategy for cancer therapy, possesses its own merits due to minimal invasiveness, lower systemic toxicity, negligible drug resistance and high efficiency [5–8]. In the last decades, PDT has been successfully testified to be effective in multiple types of cancer, such as breast, skin, oral and esophageal cancer, *etc* [9]. In PDT, photosensitizer (PS) as one of the important components could be activated by local illumination with a specific wavelength and then transforms ground-state oxygen to singlet oxygen ($^1O_2$), resulting in cancer-cell apoptosis [10]. Some common photosensitizers (PSs) including organic molecules and metalated derivatives suffer the inherent drawbacks of high hydrophobicity and poor bioavailability, hampering their photophysical and photokilling properties and limiting the subsequent clinical application [9,11]. In addition, the classic PSs with poor tumor-selectivity feature readily accumulate in the normal tissue. Therefore, maximizing the tumor-targeting efficiency still remains a major challenge in PDT.

Silicon, the most abundant mineral in the environment, has been shown to have a unique relationship with bone calcification, plant growth and positive healthy effects [12–14]. Furthermore, as the third most abundant trace element in the human body, silicon acts as an indispensable role in the body metabolic procedure and its deficiency inevitably leads to disorder and even healthy damage [13,15]. Recently,

* Corresponding author.
** Corresponding author.
*** Corresponding author.
E-mail addresses: changmeiqi1991@163.com (M. Chang), chenyuedu@shu.edu.cn (Y. Chen), zhangruifang@zzu.edu.cn (R. Zhang).

https://doi.org/10.1016/j.mtbio.2022.100393
Received 7 June 2022; Received in revised form 30 July 2022; Accepted 2 August 2022
Available online 12 August 2022

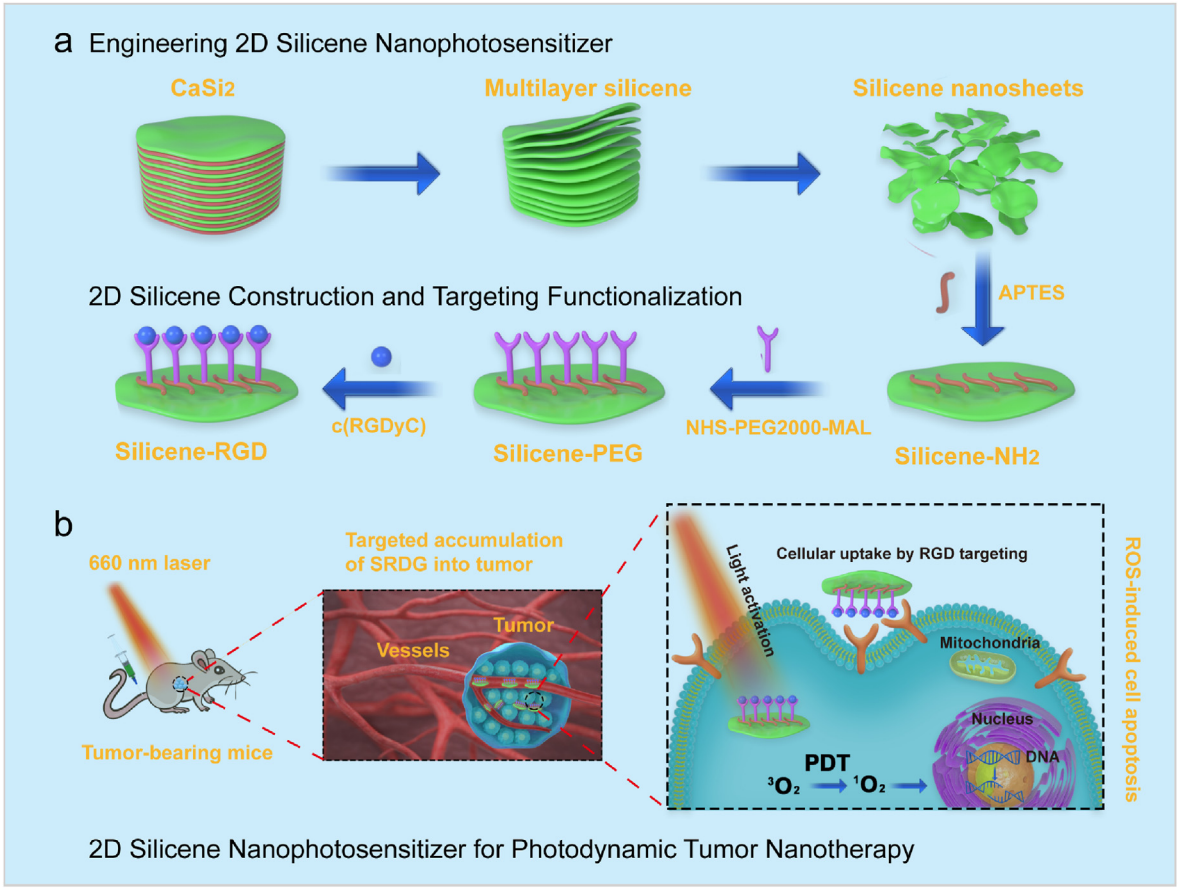

Scheme 1. (a) Scheme of the synthetic procedure of silicene nanosheets and silicene-RGD (SRGD). (b) SRGD-stimulated $^1O_2$ burst results in initiate mitochondrial damage and cell apoptosis for photodynamic tumor therapeutics.

silicon and silica nanoparticles have been extensively and deeply investigated in biological and nanocatalysis applications due to their high biocompatibility, biodegradability and biosafety in living system [16–19]. Silicene nanosheets, emerging as a new two dimensional (2D) crystalline silicon form with low buckled hexagonal honeycomb structure, would broaden perspectives for applications of silicon-based nanomaterials due to their unparalleled physiochemical merits like Quantum spin Hall effect, giant magnetoresistance and chiral superconductivity [20–22]. Recently, the development of novel synthetic strategy (wet-chemical synthesis) of 2D silicene breaks through the limitation of the large-scale/high-quality production, exhibiting intriguing prospective in biological field [23]. Moreover, the exploration of silicene opens up the possibility for next-generation nanoelectronic and nano-optoelectronic devices due to the excellent electronic and optoelectronic properties [24,25]. In recent years, 2D inorganic nanomaterials, such as graphene, black phosphorus nanosheets, transition metal carbides/carbonitrides (MXene) have aroused the extensive attentions of researchers due to its special 2D-layered structure and unique physicochemical properties [26]. Based on the high biocompatibility, excellent singlet oxygen quantum yield and efficient photodynamic therapeutic effect, they have been explored in the biomedical field with promising application potentials, especially in tumor photothermal therapy and photodynamic therapy (PDT) [27–29]. Silicene nanosheets as a new family member of 2D theranostic nanosystems also possess outstanding advantages in biomedicine. The large surface area provides abundant anchoring sites for loading either organic molecules or functional nanoparticles. The intrinsic physiochemical properties such as unique photonic response in near infrared (NIR) biowindow endow silicene nanosheets with distinct therapeutic functionality and modality. The main component of silicon in silicene nanosheets guarantees high biocompatibility and fact biodegradation, superior to other 2D biomedical nanosystems such as MoS_2, black phosphorus, and MnO_2 nanosheets [30]. Therefore, the miraculous properties and few reports focusing on biomedical applications of silicene inspire our interest to investigate the capability of $^1O_2$ generation for further PDT-based biomedical applications, which has not been achieved so far.

Herein, 2D silicene nanosheets were engineered via the liquid mild oxidation and delamination process based on the wet-chemical synthetic strategy with Zintl-phase $CaSi_2$ as the bulk silicon source [23,31] (Scheme 1a). The $CaSi_2$ precursor, iodine (I_2) and anhydrous acetonitrile (CH3CN) were added to round bottom flask, then stirred for 2 weeks at room temperature under Ar atmosphere condition. Subsequently, the products were treated ultrasonically for 12 h in ice bath and the supernatant containing silicene nanosheets was collected. The silicene nanosheets exhibit superior $^1O_2$ generation capability under the 660 nm laser irradiation, demonstrating their intriguing application in tumor PDT. After surface functionalization with a tumor-targeting agent c (RGDyC), the silicene nanosheets specifically accumulated into the tumor site. Both *in vitro* and *in vivo* results evidence the remarkable anticancer effect and desirable photoacoustic imaging performance of c (RGDyC)-grafted silicene nanosheets (denoted as SRGD). In addition, excellent biocompatibility and biosafety of SRGD further guarantee its possibility in clinical translation (Scheme 1b).

2. Results and discussion

2.1. Synthesis and structure characterization of 2D silicene nanosheets

The standalone silicene nanosheets were synthesized via the typical sequential mild oxidation and delamination processes [23,31]. Briefly,

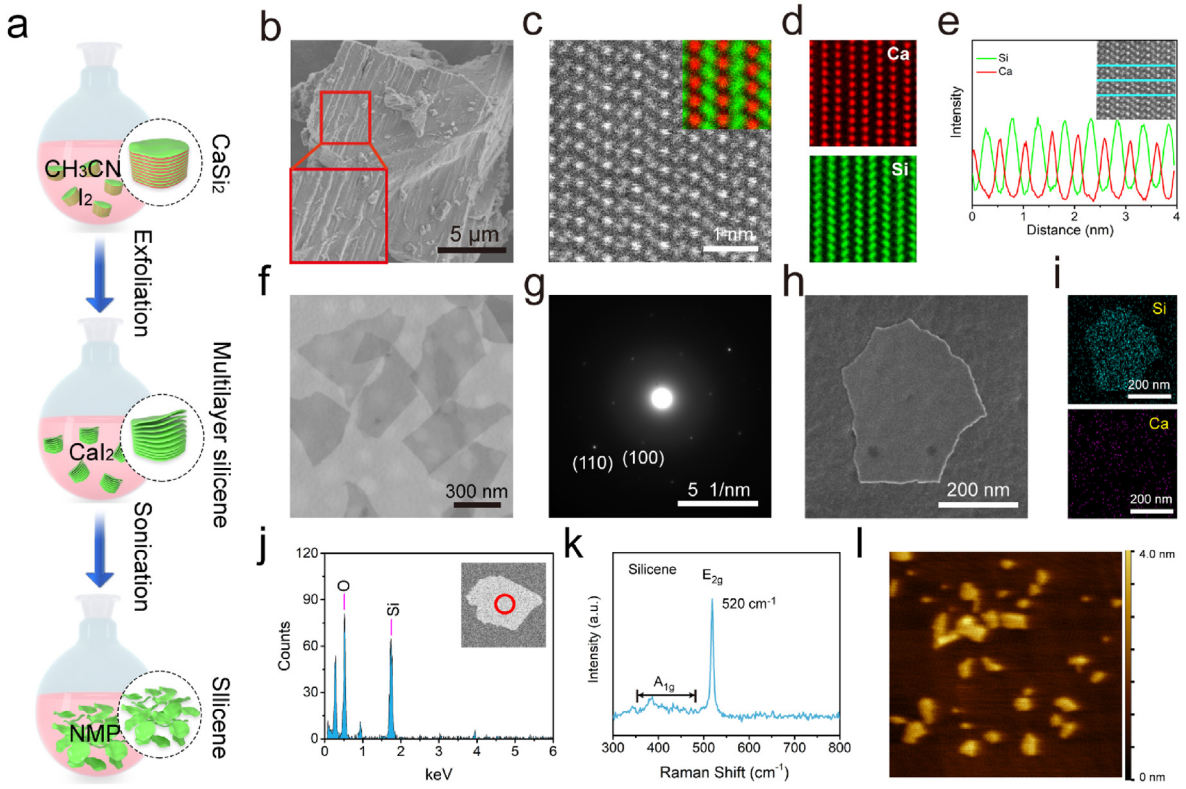

Fig. 1. Characterization of the $CaSi_2$ precursor and silicene nanosheets. (a) Schematic illustration of the synthetic procedure of silicene nanosheets. (b) SEM image and (c) HRTEM (inset: elemental mapping of overlay Ca and Si) of $CaSi_2$ precursor. (d) Elemental mappings of Ca and Si elements in $CaSi_2$. (e) Line scan element analysis of $CaSi_2$ (inset: the region of line scanning in HRTEM). TEM images in (f) bright field mode, (g) SAED pattern, (h) secondary-electron imaging mode and (i) the corresponding elemental mappings of silicene nanosheets. (j) EDS (inset: the red cycle represents selected region), (k) Raman spectrum and (l) AFM image of silicene nanosheets. (For interpretation of the references to colour/colour in this figure legend, the reader is referred to the Web version of this article.)

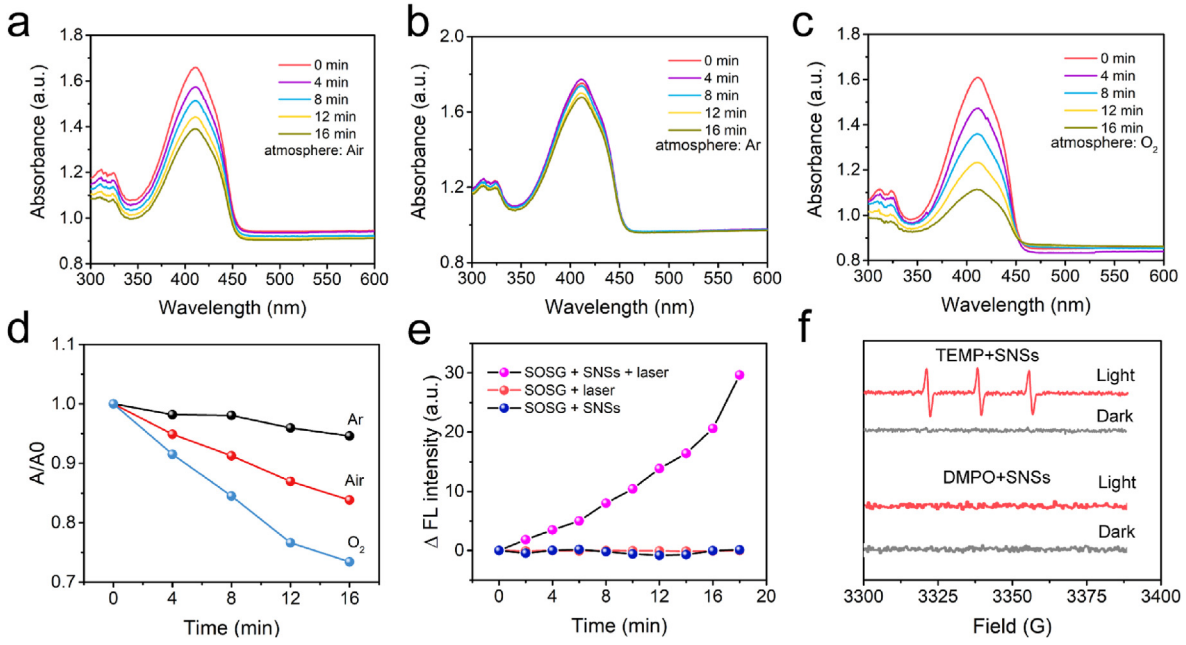

Fig. 2. Characterization of the production of singlet oxygen. (a–c) Time-dependent absorbance of DPBF in (a) Air, (b) Ar and (c) O_2 atmosphere in the presence of silicene nanosheets (50 μg·mL^{-1}) under 660 nm laser (500 mW·cm^{-2}) irradiation. (d) The normalized absorption spectra of DPBF in various atmosphere in the presence of silicene nanosheets after continuously irradiated with 660 nm (500 mW·cm^{-2}) laser. (e) Time-dependent fluorescence emission intensity detection of SOSG at 525 nm induced by silicene nanosheets (SNSs) (50 μg·mL^{-1}) and 660 nm laser (500 mW·cm^{-2}) in an ethanol solution with excitation at 488 nm. (f) ESR spectra of singlet oxygen (up) and ·OH (down) trapped by TEMP and DMPO, respectively, upon irradiation of silicene nanosheets (50 μg·mL-1) for 5 min by 660 nm laser (500 mW·cm-2).

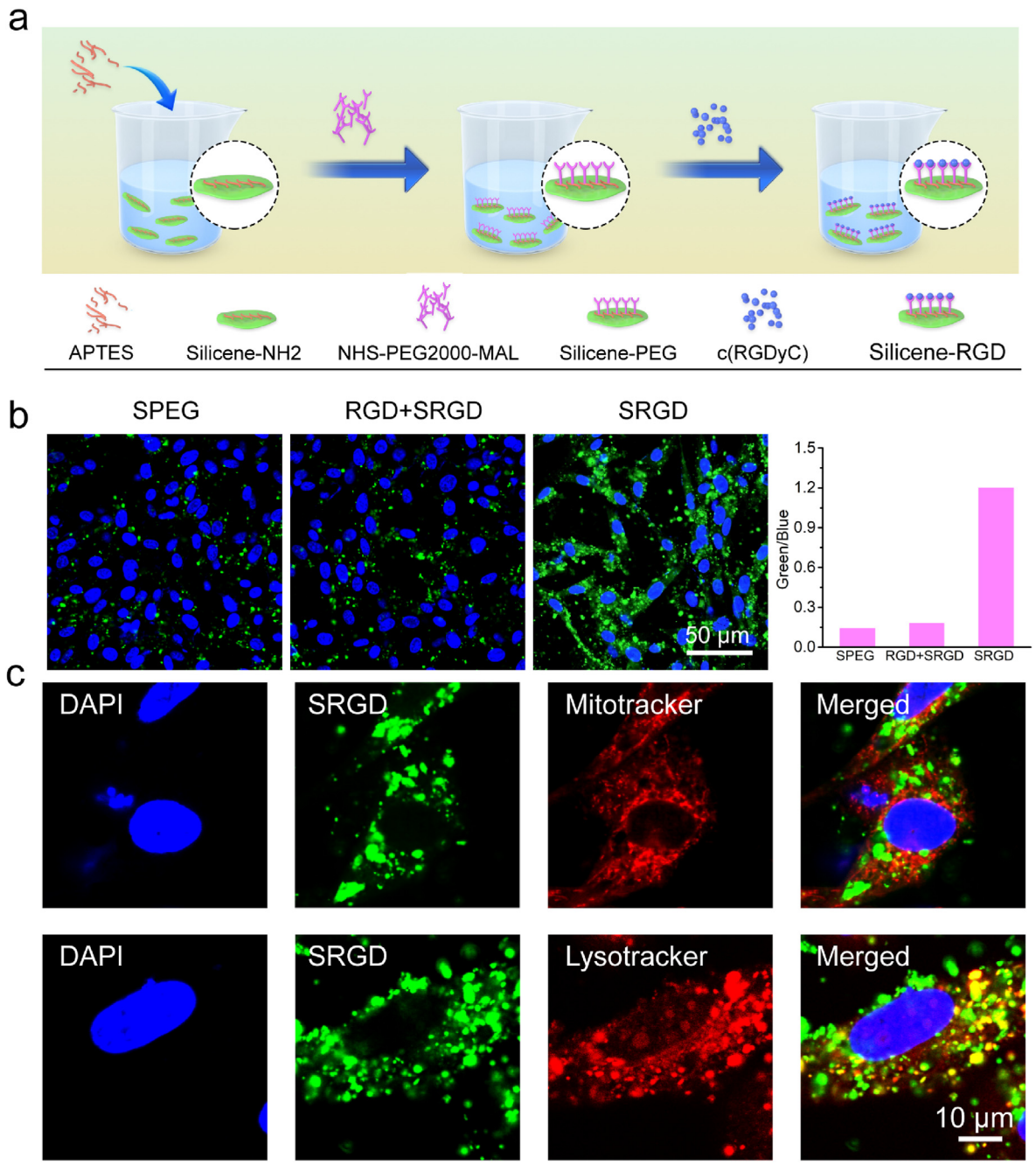

Fig. 3. Cell endocytosis and colocalization. (a) Schematic diagram of surface functionalization of silicene nanosheets. (b) CLSM imaging and quantitative analysis of U87-MG cells incubated with SPEG (Si: 50 μg·mL^{-1}) or SRGD (Si: 50 μg·mL^{-1}) for 4 h. The cells in RGD + SRGD group were pretreated with adequate free RGD following incubation with SRGD. (c) Colocalization images of U87-MG cells upon incubation with FITC-labeled SRGD for 4 h. DAPI was used to label cell nucleus. Green channel is originated from the FITC-labeled SRGD. MitoTracker Red and LysoTracker Red (red channel) were utilized to co-stain mitochondria and lysosome, respectively. (For interpretation of the references to colour/colour in this figure legend, the reader is referred to the Web version of this article.)

the Si layers of $CaSi_2$ were oxidized by a weak oxidant, I_2, in CH_3CN under Ar atmosphere protection to weaken the electrostatic interaction between the alternately stacked Ca layers and Si layers. Both excess I_2 and by-product CaI_2 could be easily removed due to their considerable solubility in CH_3CN. After the reaction process for two weeks, the intermediate products were redispersed in 1-methyl-2-pyrrolidone (NMP) and sonicated in an ice bath to obtain high-quality pristine silicene nanosheets with freestanding morphology, which facilitated the further practical applications of silicene nanosheets (Fig. 1a).

Scanning electron microscopy (SEM) images demonstrate the alternately layered stacking structure of $CaSi_2$ bulk materials, promising the feasibility of peeling out Si layers from the bulk $CaSi_2$ (Fig. 1b and inset). High-resolution transmission electron microscopy (HRTEM) images with atomic resolution clearly exhibit that the $CaSi_2$ precursors are consist of alternating hexagonal Si bilayer and trigonal Ca monolayer (Fig. 1c and inset). Unlike graphene with a perfect planar hexagonal rings, the atomic arrangements of Si in $CaSi_2$ indeed form a buckled hexagonal honeycomb structure [32]. The corresponding element mapping and line scan element analysis further confirm the alternately Ca atoms and hexagonal 2D Si atoms layers (Fig. 1d and e and inset). The Si layers were gently oxidized by I_2 under Ar atmosphere protection and the by-product in CH_3CN was removed after two weeks. Bright-field TEM image verifies the well prepared ultrathin silicene nanosheets, which features the typical 2D freestanding morphology (Fig. 1f). The selected area electron

diffraction (SAED) pattern indicates the hexagonal structure of silicene nanosheets, implying the well preserved honeycomb framework structure of silicon atoms in $CaSi_2$ (Fig. 1g). The disappearance of Ca element reflected in the element distributions demonstrates the complete removal of Ca layers and byproducts CaI_2 in the final product (Fig. S1, Supporting Information, Fig. 1h and i). Similar to the element distribution results, the energy dispersive spectroscopic (EDS) analysis shows the disappearance of intense peaks of Ca element in comparison with $CaSi_2$ (Fig. 1j and inset).

X-ray photoelectron spectroscopy (XPS) was utilized to further affirm the composition of 2D silicene nanosheets. The XPS spectrum of silicene nanosheets shows the disappearance of Ca-related peak compared to that of $CaSi_2$, further testifying the complete removal of Ca atoms (Fig. S2, Supporting Information). Moreover, Raman spectroscopy was performed to verify the integrity of silicene lattice (Fig. 1k). The typical symmetric stretching of Si–Si bonds in planar hexagons is responsible for E_{2g} vibrational modes, which generates a sharp and intense peak located at about 520 cm^{-1}. In addition, the Raman spectrum of silicene has a signature of broad asymmetric shoulder around 400-500 cm^{-1} (A_{1g} breathing mode), which is induced by vertical buckling, in contrast to bulk silicon and $CaSi_2$ [33]. The morphology of as-synthesized silicene nanosheets was further tested by atomic force microscopy (AFM), which clearly illustrates the typical 2D layer structure of standalone silicene nanosheets with lateral size ranging from 90 to 250 nm and thickness distributing from 0.7 to 3.5 nm, respectively (Figure 1l and Fig. S3, Supporting Information).

2.2. Photodynamic property of silicene nanosheets

As a graphene analogue of silicon, the silicene nanosheets are anticipated to generate $^1O_2$ under laser irradiation. Herein, the 1, 3-diphenylisobenzofuran (DPBF) was adopted as probe to monitor $^1O_2$ generation of silicene nanosheets. As shown in Fig. 2a, the UV–vis absorption values at 410 nm exhibit a time-course decrease under 660 nm laser (500 $mW{\cdot}cm^{-2}$) irradiation with the presence of silicene nanosheets, implying $^1O_2$-dependent DPBF oxidation process. Furthermore, the photodegradation performance of DPBF in Ar/O_2 atmosphere was also investigated to detect the effect of atmosphere species on the production of $^1O_2$ (Fig. 2b and c). As expected, the absorbance spectra of DPBF show an inconspicuous change under Ar condition but remarkably decrease in oxygen environment, which clearly reveals the oxygen- and light-dependent photodynamic features of silicene nanosheets (Fig. 2d and Fig. S4, Supporting Information). Singlet oxygen sensor green reagent (SOSG) was also selected as the molecular probe for fluorescence detection to evaluate $^1O_2$ generation capability of silicene nanosheets. The fluorescence intensity of SOSG gradually increased with the prolonged exposure time to 660 nm laser in the presence of silicene nanosheets, further confirming $^1O_2$ generation (Fig. 2e). Finally, electron spin resonance (ESR) spectroscopy was conducted to capture direct evidence of reactive oxygen species (ROS) generated from silicene upon 660 nm laser irradiation. Herein, 2,2,6,6-tetramethylpiperidine (TEMP) and 5,5-Dimethyl-1-pyrroline *N*-oxide (DMPO) were utilized as $^1O_2$ and •OH (or $O_2^{\bullet-}$) trappers, respectively. The $^1O_2$ spectrum with 1:1:1 triplet signal characteristic was captured and observed only under laser irradiation, while neither ·OH nor $O_2^{\bullet-}$ signals was detected (Fig. 2f). It can be interpreted that the electrons in silicene nanosheets are excited from ground state to the excited singlet state after 660 nm laser irradiation, followed by $^1O_2$ generation from the ground state $^3O_2$ on the silicene nanosheet accompanying with the electron transferring from the excited singlet state to the ground state.

To investigate the generation ability of $^1O_2$, Anthracene-9,10-dipropionic acid disodium salt (Na_2-ADPA) and Rose Bengal (RB) were selected as indicator agent and standard photosensitizer ($^1O_2$ quantum yield of RB is 0.75 in water) for the calculation of $^1O_2$ quantum yield, respectively [34]. The absorption values at 378 nm of Na_2-ADPA aqueous solution decrease in the presence of silicene or RB upon the 660 nm laser irradiation, indicating the efficient generation of $^1O_2$ by silicene and RB (Fig. S5, Supporting Information). Simultaneously, the $^1O_2$ quantum yield of silicene was calculated to be 0.61, revealing similar $^1O_2$ production capacity compared to RB.

In addition, the photostability of silicene was estimated considering the photobleaching problem of traditional photosensitizer. The absorbance of silicene at 410 nm displayed a negligible change after exposure to 660 nm laser for 90 min, revealing the outstanding photostability of silicene and giving a promising future for biomedical applications (Fig. S6, Supporting Information).

2.3. Cancer cellular endocytosis, targeting potency and colocalization assay

To further improve the biocompatibility and tumor-targeting properties for favoring subsequent therapeutic applications, silicene was ammoniated with silane coupling agent (denoted as silicene-NH_2) followed by successive conjugation of polyethylene glycol (denoted as SPEG) and c (RGDyC) peptides (denoted as SRGD) (Fig. 3a). The grafting processes of –NH_2, PEG, and c (RGDyC) were monitored by Zeta potential, which exhibited serial changes resulting from the positive charge of –NH_2 and slight negative charge on the surface of PEG and RGD, respectively (Fig. S7a, Supporting Information). The Fourier transform infrared spectrometer (FT-IR) spectral analysis results showed that the absorption band of SRGD at 1634 cm^{-1} was present compared with silicene nanosheets, which is consistent with the existence of carbonyl groups in RGD, confirming that the targeted moieties are coupled on silicene nanosheets (Fig. S7b, Supporting Information). Subsequently, fluorescein isothiocyanate (FITC)-labeled SRGD (FITC-SRGD) was prepared for confocal laser scanning microscopy (CLSM) imaging to investigate the U87-MG cancer cellular endocytosis of SRGD. The gradually enhanced green fluorescence signals of FITC-SRGD were observed with prolonged incubation time, indicating increasing efficient accumulation of SRGD in U87-MG cells and time-dependent cellular internalization process (Fig. S8, Supporting Information).

RGD peptide could selectively recognize and bind to $\alpha_v\beta_3$ integrin, which is overexpressed in angiogenesis and metastases process of cancer [35]. To demonstrate the targeting property of RGD, FITC-SPEG and FITC-SRGD were incubated with U87-MG cells featuring overexpressed $\alpha_v\beta_3$ integrin level for 4 h. As shown in Fig. 3b, the fluorescence signal intensity of FITC-SRGD group is stronger than that of FITC-SPEG group. Moreover, as a complementary but indispensable method, the pre-blocking experiment was designed to further testify the cancer cell-targeting ability of SRGD. U87-MG cells were treated with FITC-SRGD after pre-incubation with free RGD for 1 h, displaying much weaker fluorescence signal than that of without pre-blocking treatment, which is attributed to the specific binding of RGD and overexpressed $\alpha_v\beta_3$ integrin. The above results provide concrete evidences in support of the target specificity of RGD moieties. Furthermore, the intracellular trace of SRGD in subcellular organelles level was further tracked. U87-MG cells were co-incubated with FITC-SRGD and organelle-targeted fluorescent probes (mitochondria-MitoBright Red, lysosomes-LysoTracker Red, cell nucleus-DAPI). The merged yellow fluorescence in CLSM image indicates the efficient co-localization of SRGD within lysosomes. Comparatively, no significant co-localization processes of SRGD in mitochondria and cell nucleus can be detected (Fig. 3c). These results manifest that $\alpha_v\beta_3$ integrin receptor-mediated endocytosis is an essential pathway in the cellular uptake process of SRGD.

2.4. In vitro photodynamic therapeutic efficiency

Benefiting from the highly efficient $^1O_2$ generation of silicene and specific interaction of SRGD with $\alpha_v\beta_3$ integrin, the *in vitro* cytotoxicity and photodynamic therapeutic effects were initially investigated on U87-MG cells. The biosafety evaluation of SRGD, with an increasing concentration from 25 $\mu g{\cdot}mL^{-1}$ to 400 $\mu g{\cdot}mL^{-1}$, was performed by standard

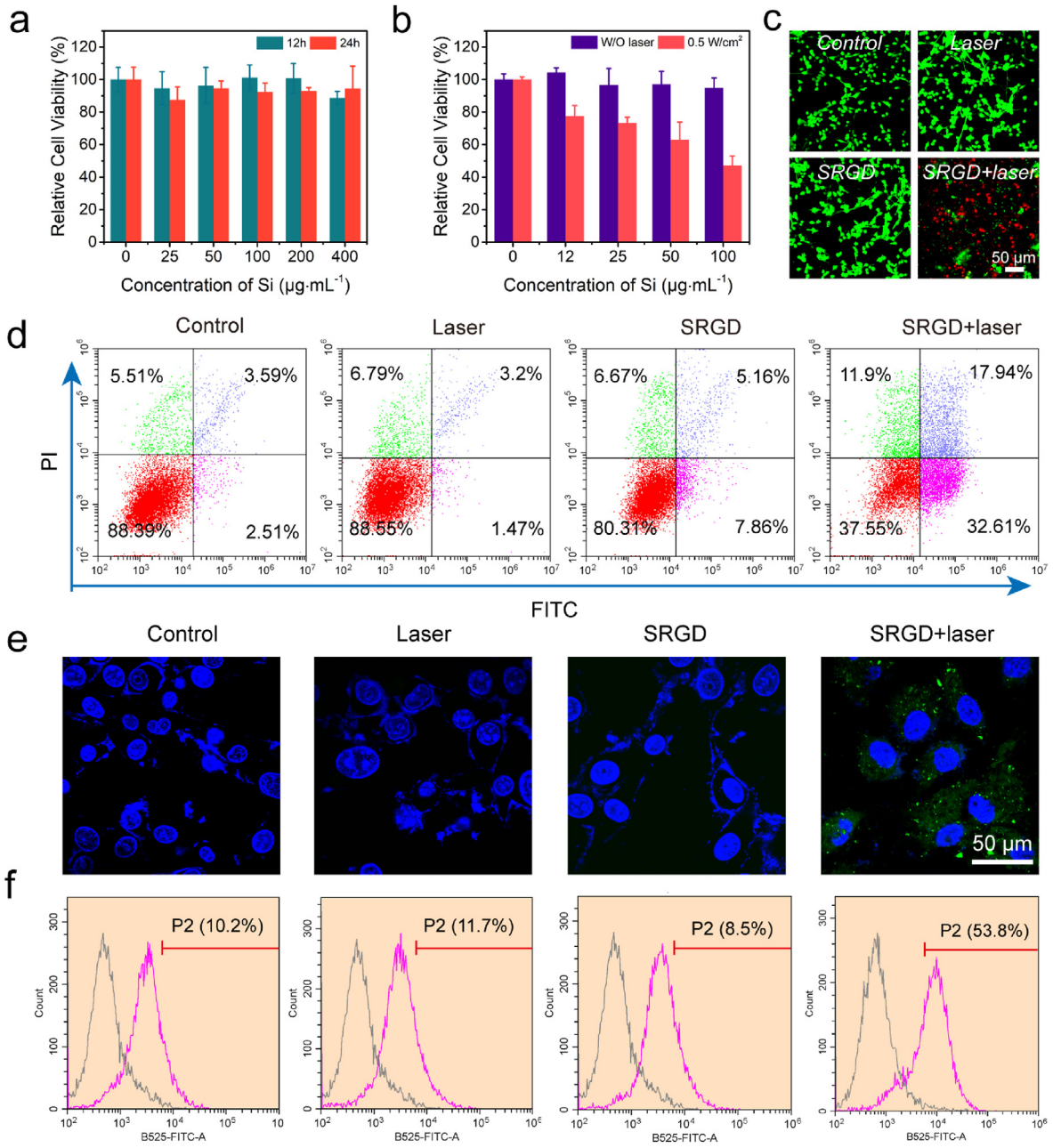

Fig. 4. ***In vitro*** **photodynamic therapy and ROS detection.** (a) Cytotoxicity of SRGD with various concentrations after incubated with U87-MG cells for 12 h and 24 h, respectively. (b) Relative viability of U87-MG cells after incubation with different concentrations of SRGD for 4 h followed by irradiation with 660 nm laser (500 mW·cm^{-2}) for 15 min. (c) CLSM imaging of U87-MG cells treated with control, laser, SRGD and SRGD + laser group, respectively. Calcein-AM/PI kit was employed to stain live (green fluorescence) and dead (red fluorescence) cells. (d) Flow cytometry analysis results of U87-MG cells treated with different groups. (e) CLSM imaging and (f) flow cytometry analysis were performed to detect the ROS generation of U87-MG cells after incubation with SRGD and followed by 660 nm laser irradiation for 15 min. (For interpretation of the references to colour/colour in this figure legend, the reader is referred to the Web version of this article.)

CCK-8 assays after incubation with U87-MG cells in dark for 12 h and 24 h, respectively. The results demonstrate that SRGD exhibits negligible negative effect on U87-MG cells, with cell viability above 90% after co-incubation for 24 h at high concentration of 400 μg·mL^{-1} (Fig. 4a). In contrast, a significant lower cell viability was obtained after incubation with SRGD for 4 h followed by 660 nm laser irradiation (500 mW·cm^{-2}, 15 min), and only about 47% of cells survived at a concentration of 100 μg·mL^{-1} (Fig. 4b). In addition, the photothermal effect of SRGD in inhibiting cell proliferation was excluded due to the negligible temperature elevation (Fig. S9, Supporting Information). These results indicate cell proliferation ability was significantly inhibited with the increasing concentration of SRGD in the presence of 660 nm laser, displaying excellent biocompatibility and *in vitro* high-efficiency photodynamic therapeutic performance of SRGD. Moreover, the U87-MG cell-killing effect after different treatments was visualized through live/dead double-staining assay. CLSM imaging of SRGD + laser group clearly displays the dead cells resulting from phototoxicity of SRGD under laser irradiation, while other treatments show almost no visible red fluorescence (Fig. 4c). To more accurately evaluate the apoptosis of U87-MG cells, the flow cytometry analysis was performed after various treatments. As shown in Fig. 4d, SRGD and laser combined treatment (SRGD + laser) group resulted in apparent cell apoptosis with the higher late apoptosis ratio, approximately 50%, than that of control, laser and SRGD groups (approximately 5%, 5% and 13%, respectively). As a consequence, it can

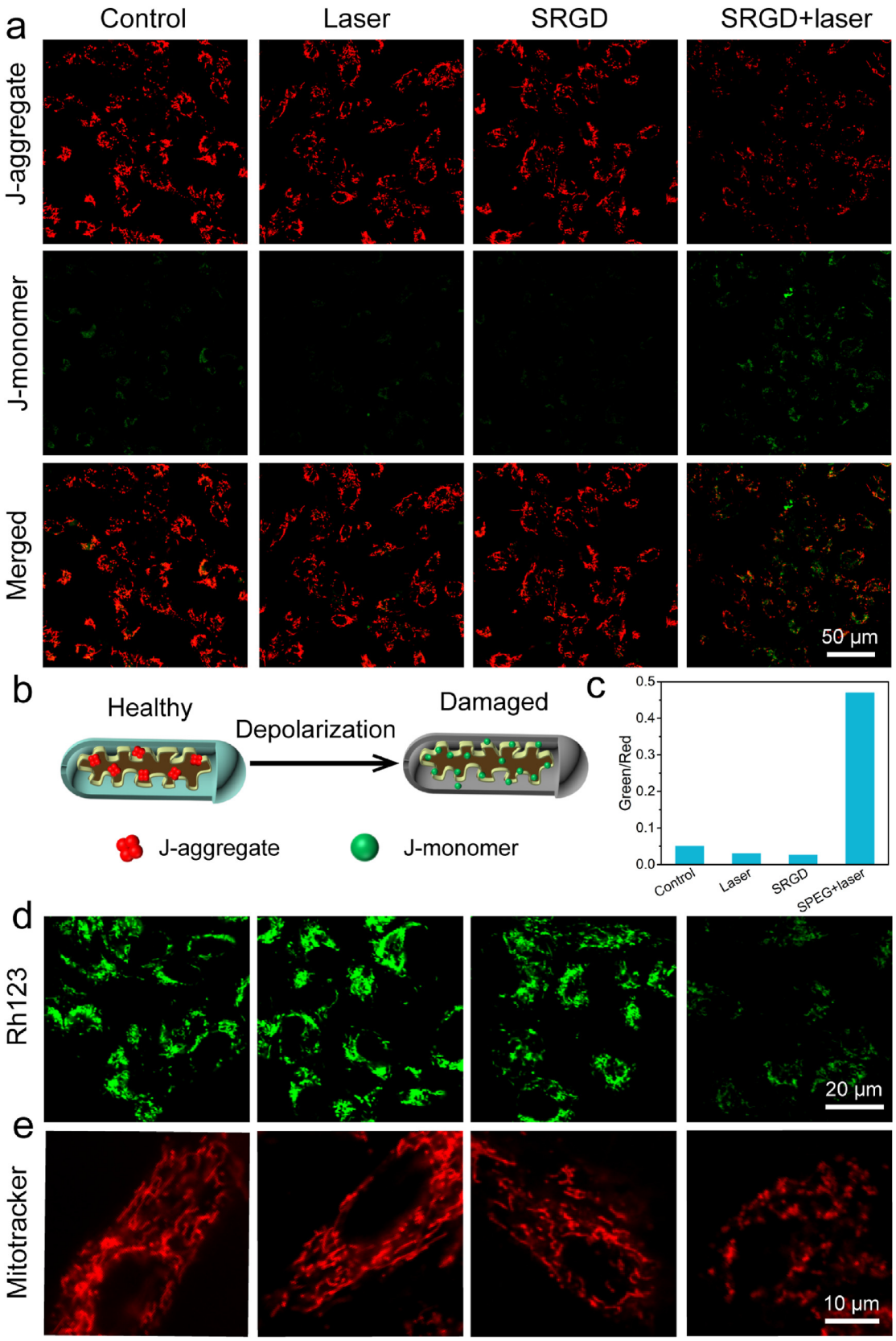

Fig. 5. Mitochondrial damage of U87-MG cells induced by singlet oxygen. (a) CLSM imaging of JC-1 stained U87-MG cells after varying treatments for the evaluation of mitochondrial membrane potential changes (b) Schematic of mitochondrial damage and fluorescence imaging, and (c) quantitative analysis of mitochondrial membrane potential. (d) ATP level in U87-MG cells evaluated by Rh 123 staining following different treatments. (e) CLSM imaging of mitochondrial morphology changes in U87-MG cells after treated with different groups. The cells were stained with MitoTracker Red. (For interpretation of the references to colour/colour in this figure legend, the reader is referred to the Web version of this article.)

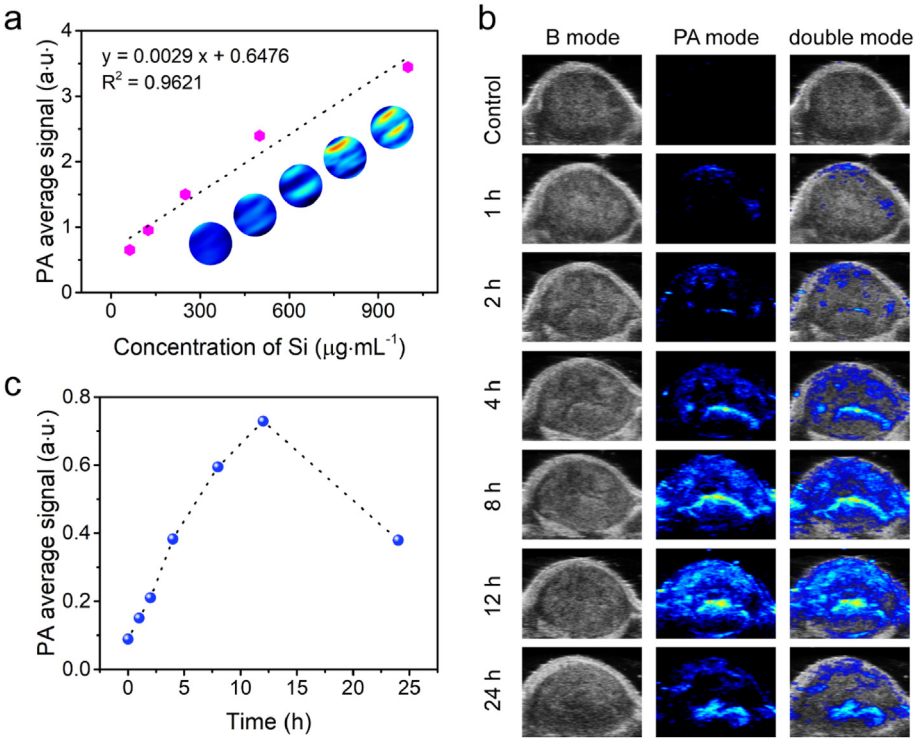

Fig. 6. (a) The linear correlation of *in vitro* PA signal intensity and the concentrations of SRGD (Si: 1000, 500, 250, 125, 62.5 μg·mL^{-1}) (inset: the corresponding PA images). (b) Time-course *in vivo* PA images of B mode, PA mode and double mode of tumor at various time points after the intravenous injection with SRGD (15 mg·kg^{-1}) and (c) the corresponding PA signal values by quantitative analysis.

be inferred that SRGD with potent cytotoxicity may play a significant role in photodynamic cancer therapy.

To further explore the intrinsic mechanism of SRGD-induced apoptosis in U87-MG cells, 2′,7′-Dichlorodihydrofluorescein diacetate (DCFH-DA) was adopted as probe to detect the generation of ROS in U87-MG cells. CLSM images reveal minimal green fluorescence in U87-MG cells under the 660 nm laser irradiation (laser group) or in the presence of SRGD only (SRGD group) compare to that of untreated cells (control group), while bright green fluorescence was monitored in SRGD + laser group, demonstrating the generation of ROS induced by light-motivated photodynamic effect of SRGD (Fig. 4e). Subsequently, the flow cytometry was conducted to quantitatively analyze the ROS yield in U87-MG cells of control, laser, SRGD and SRGD + laser groups (Fig. 4f). As expected, the level of ROS in U87-MG cells was upregulated only in SRGD + laser group, while SRGD and laser groups performed similarly in contrast to control group. The intracellular ROS signal was substantially amplified by SRGD under laser irradiation, offering the reliable support for further *in vivo* highly efficient photodynamic anti-cancer treatment.

2.5. ROS-induced mitochondrial damage

Mitochondria as mobile organelles take a central role both in adenosine triphosphate (ATP) metabolism and regulation of apoptosis [36]. Excess ROS indirectly initiate the permeability transition pore opening and respiratory chain damaging in mitochondria, which lead to the increase of mitochondrial membrane permeability and loss of mitochondrial membrane potential, releasing the pro-apoptotic factors such as apoptosis-inducing factor and cytochrome *c*, and ultimately inducing apoptosis [37,38]. Mitochondrial dysfunction induced by SRGD was studied in a method of mitochondrial membrane potential evaluation. JC-1 could transform into red J-aggregate after entering the mitochondria with physiological function, while the green JC-1 monomers appear in dysfunctional mitochondria. Herein, JC-1 was selected as the fluorescence probe to stain U87-MG cells with various treatments for further observation. Distinguishing from control, laser and SRGD groups, the markedly reduced red fluorescence and increased green fluorescence were observed in SRGD + laser group, implying the loss of mitochondrial membrane potential (Fig. 5a, b and c). Furthermore, Rh123 probe as ATP content indicator exhibits yellowish green fluorescence due to membrane penetration characteristics and mitochondrial aggregation properties [39]. As expected, the fluorescence intensity of SRGD + laser group visibly decreased in contrast to other groups after staining with Rh123 (Fig. 5d). These results confirm that SRGD combined laser irradiation treatment would lead to mitochondrial depolarization, decrease ATP production, and consequently induce cancer cell apoptosis.

The equilibrium state of fission and fusion is the pivotal dynamic process in maintaining mitochondrial morphology, integrity, network structure and physiological functions [40]. Fission contributes to the fragmentation of mitochondria and creating smaller and more discrete pieces, while fusion is responsible for interconnected network morphology [41]. In order to observe the mitochondrial morphology change, U87-MG cancer cells were stained with the mitochondria tracer (MitoBright Red) after treating with different strategies. The mitochondria maintain the integrated tubular interconnected network morphology in control, laser and SRGD groups, while SRGD + laser group induces the mitochondrial fragmentation, elucidating enhanced mitochondrial fission (Fig. 5e). The increased fission process causes mitochondrial dysfunction and consequently apoptosis by releasing cytochrome *c* [42]. Based on the above results, it can be determined that ROS-induced mitochondrial function impairment is a major mechanism of cell apoptosis.

2.6. In vitro and in vivo photoacoustic imaging

Photoacoustic (PA) imaging enables the conversion of the thermoelastic waves that are induced by photons in tissue into images, featuring with higher resolution, deeper tissue penetration, more sensitive and richer optical contrasts compared to traditional optical imaging, which

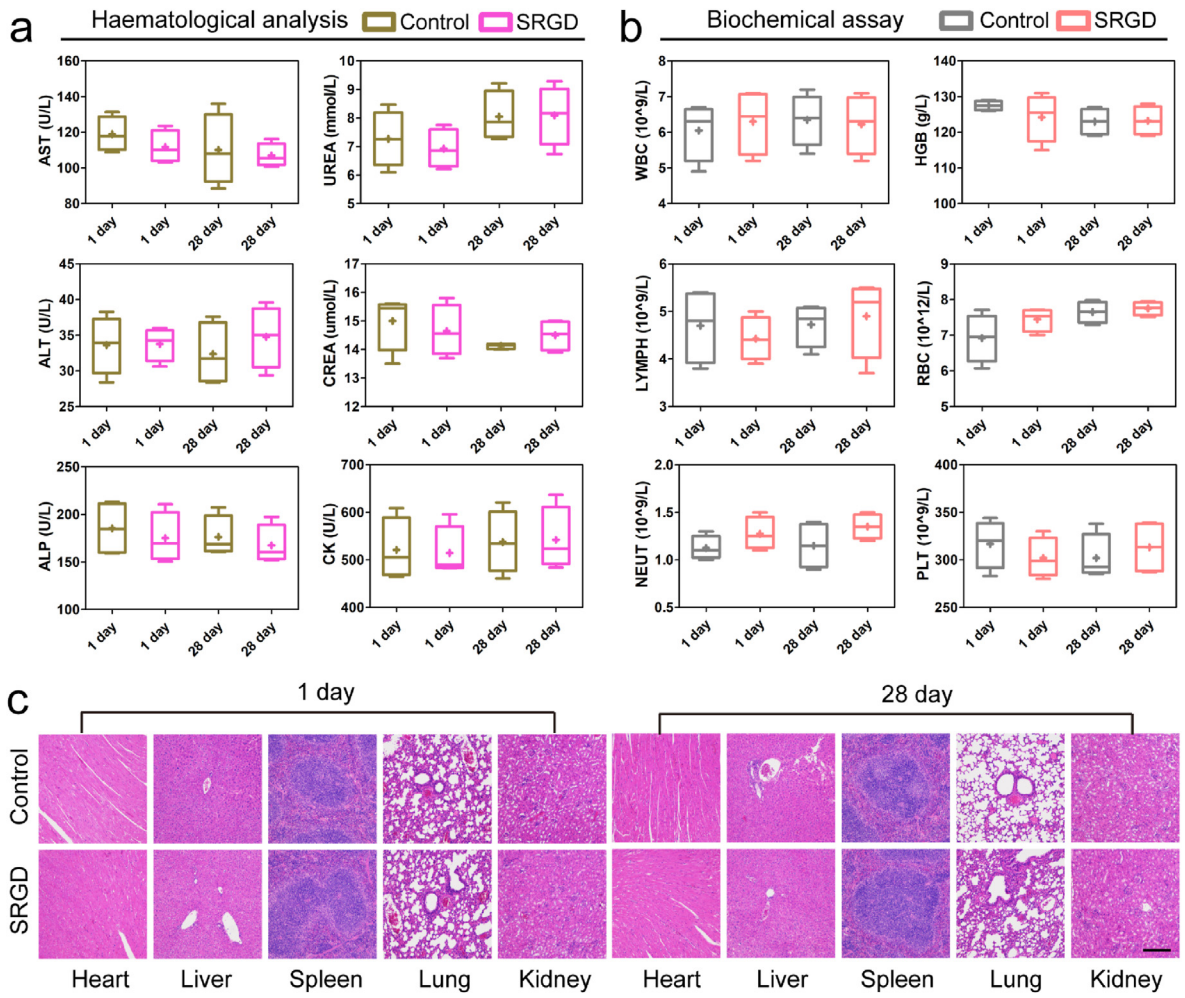

Fig. 7. (a) Standard haematological analysis and (b) serum biochemical assay. (AST, glutamic oxaloacetic transaminase; ALT, alanine transaminase; ALP, alkaline phosphatase; UREA, urea; CREA, Creatinine; CK, creatine kinase; WBC, white blood cell; LYMPH, lymphocyte; NEUT, neutrophil; HGB, hemoglobin; RBC, red blood cell; PLT, platelets). Mean values and error bars are presented as mean ± SD. (c) Histological examination (H&E staining) of heart, liver, spleen, lung and kidney dissected from the mice on the 1st and 28th day after intravenous injection of SRGD (20 mg·kg^{-1}). Scale bar: 200 μm. (For interpretation of the references to colour/colour in this figure legend, the reader is referred to the Web version of this article.)

plays a crucial role in early detection and precise location/monitoring of tumor [43]. To investigate PA imaging capability of SRGD, *in vitro* imaging was initially performed by Vevo LAZR photoacoustic imaging system. SRGD aqueous solutions with different concentrations were imaged and the PA signal at 950 nm near infrared light excitation were recorded (Fig. 6a). A good linear correlation ($R^2 = 0.9621$) between the SRGD content and the corresponding PA signal intensity proved that SRGD could be the desirable candidate as a contrast agent for PA imaging. For *in vivo* PAI, the U87-MG tumor bearing mice were injected intravenously with SRGD nanomedicines, and then two dimensional ultrasound and PA images of tumor were acquired at predetermined time point followed by the PA signals analysis (Fig. 6b and c). The tumor exhibited gradually enhanced PA signal in 12 h post-injection of SRGD in contrast to control group (without injection of SRGD). Remarkably, the PA signal in tumor showed about 9-times greater than that of control group at 12 h post-injection, illuminating excellent passive intratumoral accumulation and longer retention time in tumor tissues of SRGD. It is expected that the PA imaging property of SRGD could provide guidance for tumor detection and location.

2.7. *In vivo* biocompatibility and metabolism

To interrogate *in vivo* biocompatibility and biosafety concerns of SRGD, female Kunming mice (4 weeks) were injected with SRGD. On day 1 and day 28 post injection, the whole blood haematological analysis and serum biochemical assay were performed to detect the *in vivo* toxicity of SRGD. All indicators of SRGD groups demonstrate no significant difference compared with those of control groups, indicating SRGD have negligible acute and chronic toxicity side effects for further noninvasive therapy (Fig. 7a and b). The vital organs were dissected for histology analysis by hematoxylin & eosin (H&E) staining, which showed no distinct inflammation, necrosis and fibrosis lesions, implying insignificant cardiotoxicity, hepatic/spleen/lung injury and renal toxicity (Fig. 7c).

Considering the biodegradability concern, the metabolism of SRGD *in vivo* was investigated by inductively coupled plasma optical emission spectrometer (ICP-OES). After 48 h post-injection, a large proportion of silicon element was excreted from mice body through urine and faeces, exhibiting excellent biodegradability in physiological environment (Fig. S10, Supporting Information), further evidencing that the injectable SRGD is a biocompatible and degradable 2D nanomedicine.

2.8. *In vivo* anticancer photodynamic therapeutics

Encouraged by the desirable *in vitro* anticancer efficacy, superior biocompatibility and biodegradability of SRGD, animal experiments were performed to exploit the *in vivo* photodynamic therapeutic efficacy. The U87-MG tumor bearing mice were divided into five groups (n = 5),

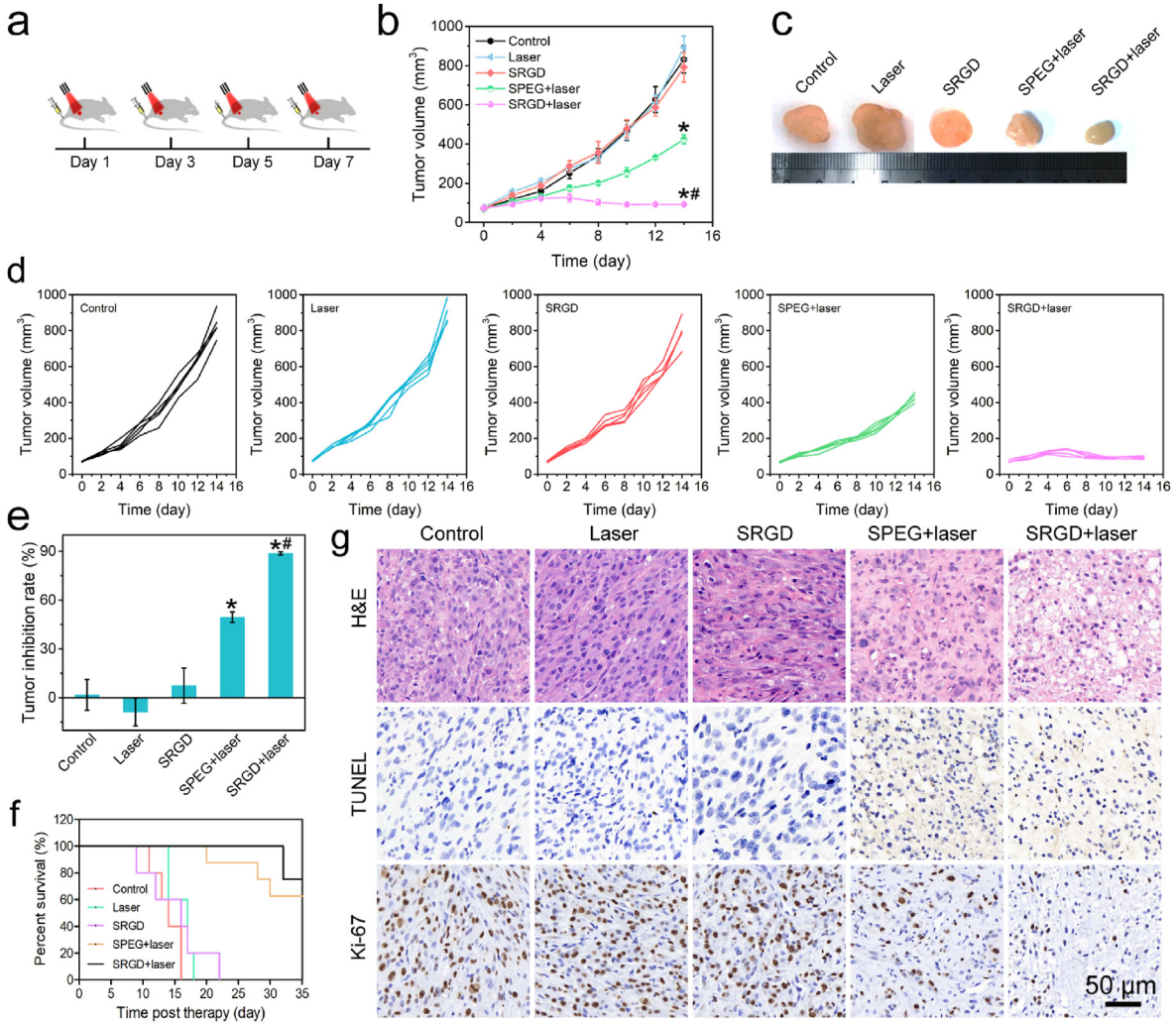

Fig. 8. ***In vivo*** **anticancer photodynamic therapeutics by SRGD.** (a) The schedule of *in vivo* treatment of SRGD (All groups received injection or laser treatment on the day 1, 3, 5 and 7, respectively). (b) Time-dependent tumor volume changes of U87-MG tumor-bearing mice after different treatments (n = 5, all the data are presented as mean ± SD). (c) Representative photographs of tumors dissected from each treatment group on day 14. (d) Individual tumor volume changes curves after different treatments. (e) The tumor inhibition of each group after 14 days of therapies (n = 5). (f) Survival analysis curve of mice in the course of 35 days after different treatments (n = 5). (g) Representative H&E, TUNEL and Ki-67 staining images of tumor tissues from each group. *P < 0.01 compared with control group, #P < 0.01 compared with SPEG + laser group.

including control, laser, SRGD, SPEG + laser and SRGD + laser. The control and SRGD groups were received intravenous injection of PBS and SRGD, respectively. For SPEG + laser and SRGD + laser groups, the mice were injected with SPEG and SRGD via the tail vein followed by 660 nm laser irradiation (500 mW·cm^{-2}, 15 min). All the treatments were performed on the first, third, fifth and seventh day, respectively (Fig. 8a). The tumor sizes were monitored and recorded every other day in the duration of therapy. The tumors of laser and SRGD groups exhibited a negligible suppression rate compared with those of control group, and SPEG + laser group showed a slight therapeutic effect. As anticipated, SRGD + laser group displayed distinct tumor growth inhibition effect, which is benefit from superior photodynamic effect of 2D silicene and the specific target ability of RGD (Fig. 8b–d and Fig. S11, Supporting Information).

Furthermore, the tumor inhibition rates of each group on the 14th day were calculated to quantitatively analyze the tumor suppression capability. The tumor inhibition rates of control, laser and SRGD groups are 1.7%, −8.8% and 7.4%, respectively. PDT derived from SPEG increased the rate to 49.5%. Comparatively, the evident inhibition rate with 88.7% has been captured in SRGD + laser group (Fig. 8e). In addition, the body weights of mice were not obviously affected by various therapies in contrast to those of control group, implying negligible adverse effects of SPEG, SRGD and laser groups (Fig. S12, Supporting Information). Finally, the survival analysis was preformed to evaluate the survival time of each group. The mice with tumor volume exceeding 1000 mm^3 were identified as death. All the mice of control, laser, and SRGD groups died on the day 16, 18 and 22, respectively. By contrast, the therapy modalities of SPEG + laser and SRGD + laser significantly prolong the living time of mice (Fig. 8f).

To analyze the pathological change of tumor tissues, the representative tumors were dissected after the last time treatment and sliced for H&E, terminal deoxynucleotidyl transferase dUTP nick end labeling (TUNEL) and Ki-67 antibody staining (Fig. 8g). H&E analysis displayed much more pyknotic cancer cells and large vacuoles in SRGD + laser group, confirming the occurrence of apoptosis or death. While the tumor tissues in control, laser, and SRGD group maintained intact morphology. Similarly, the SRGD + laser and SPEG + laser groups exhibited obvious cell apoptosis and proliferation inhibition according to TUNEL and Ki-67 staining assays. The above results further verified the striking photodynamic therapeutic efficiency of SRGD.

3. Conclusions

In summary, we have developed high-quality 2D silicene nanosheets via a facile and scalable strategy based on the wet-chemical synthetic mechanism. The silicene nanosheets demonstrated high photostability and superior $^1O_2$ generation capacity by photonic activation. Remarkably, the conjunction of c (RGDyC) and silicene nanosheets enabled SRGD nanomedicine to serve as a theranostic nanoplatform with considerable biocompatibility, achieving a potent *in vivo and in vitro* photodynamic therapeutic anticancer efficacy under the guidance of PA imaging for oncotherapy and tumor detection/monitoring. Moreover, the specific cancer cell-targeting property arising from c (RGDyC) achieved the excellent photodynamic therapeutic selectivity to the specific tumor microenvironment characterized by the overexpression of $\alpha_v\beta_3$ integrin, which further facilitated tumor growth inhibition efficiency of SRGD and avoided the negative effect on normal cells. It is highly expected that this work can offer fresh inspiration to broaden the utilization of 2D silicene nanosheets in biomedicine.

Credit author statement

Y. Chen, M. Chang and R. Zhang designed the project. H. Duan, H. Lin, H. Huang, W. Feng, W. Guo, L. Wu carried out the experiments and the characterization. H. Duan, M. Chang, Y. Chen and R. Zhang wrote and revised the paper. All authors participated in the discussions of the results.

Data availability statement

The raw/processed data required to reproduce these findings cannot be shared at this time due to technical or time limitations. Data will be made available on request.

Declaration of competing interest

The authors declare that they have no known competing financial interests or personal relationships that could have appeared to influence the work reported in this paper.

Acknowledgments

We greatly acknowledge the financial support of Shanghai Science and Technology Program (Grant No. 21010500100), Basic Research Program of Shanghai Municipal Government (Grant No. 21JC1406002), National Nature Science Foundation of China (Grant No. 81871364).

Appendix A. Supplementary data

Supplementary data to this article can be found online at https://doi.org/10.1016/j.mtbio.2022.100393.

References

[1] F. Bray, J. Ferlay, I. Soerjomataram, R.L. Siegel, L.A. Torre, A. Jemal, Global cancer statistics 2018: GLOBOCAN estimates of incidence and mortality worldwide for 36 cancers in 185 countries, CA A Cancer J. Clin. 68 (2018) 394–424.
[2] A. Albini, M.B. Sporn, The tumour microenvironment as a target for chemoprevention, Nat. Rev. Cancer 7 (2007) 139.
[3] J. Shi, P.W. Kantoff, R. Wooster, O.C. Farokhzad, Cancer nanomedicine: progress, challenges and opportunities, Nat. Rev. Cancer 17 (2017) 20.
[4] V.P. Torchilin, Multifunctional, stimuli-sensitive nanoparticulate systems for drug delivery, Nat. Rev. Drug Discov. 13 (2014) 813.
[5] D.E. Dolmans, D. Fukumura, R.K. Jain, Photodynamic therapy for cancer, Nat. Rev. Cancer 3 (2003) 380.
[6] J.P. Celli, B.Q. Spring, I. Rizvi, C.L. Evans, K.S. Samkoe, S. Verma, B.W. Pogue, T. Hasan, Imaging and photodynamic therapy: mechanisms, monitoring, and optimization, Chem. Rev. 110 (2010) 2795–2838.
[7] Q. Ma, X. Sun, W. Wang, D. Yang, C. Yang, Q. Shen, J. Shao, Diketopyrrolopyrrole-derived organic small molecular dyes for tumor phototheranostics, Chin. Chem. Lett. 33 (2022) 1681–1692.
[8] H. Dai, X. Wang, J. Shao, W. Wang, X. Mou, X. Dong, A. Orcid, NIR-II organic nanotheranostics for precision oncotherapy, Small 17 (2021), e2102646.
[9] S.S. Lucky, K.C. Soo, Y. Zhang, Nanoparticles in photodynamic therapy, Chem. Rev. 115 (2015) 1990–2042.
[10] N.L. Oleinick, R.L. Morris, I. Belichenko, The role of apoptosis in response to photodynamic therapy: what, where, why, and how, Photochem. Photobiol. Sci. 1 (2002) 1–21.
[11] R.R. Allison, G.H. Downie, R. Cuenca, X.H. Hu, C.J. Childs, C.H. Sibata, Photosensitizers in clinical PDT, Photodiagnosis Photodyn. Ther. 1 (2004) 27–42.
[12] E.M. Carlisle, Silicon: a possible factor in bone calcification, Science 167 (1970) 279–280.
[13] K. Martin, The chemistry of silica and its potential health benefits, J. Nutr. Health Aging 11 (2007) 94.
[14] N. Yamaji, G. Sakurai, N. Mitani-Ueno, J.F. Ma, Orchestration of three transporters and distinct vascular structures in node for intervascular transfer of silicon in rice, Proc. Natl. Acad. Sci. USA 112 (2015) 11401–11406.
[15] H. Ehrlich, K.D. Demadis, O.S. Pokrovsky, P.G. Koutsoukos, Modern views on desilicification: biosilica and abiotic silica dissolution in natural and artificial environments, Chem. Rev. 110 (2010) 4656–4689.
[16] C. Chiappini, E. De Rosa, J. Martinez, X. Liu, J. Steele, M. Stevens, E. Tasciotti, Biodegradable silicon nanoneedles delivering nucleic acids intracellularly induce localized in vivo neovascularization, Nat. Mater. 14 (2015) 532.
[17] Y. Deng, Y. Cai, Z. Sun, J. Liu, C. Liu, J. Wei, W. Li, C. Liu, Y. Wang, D. Zhao, Multifunctional mesoporous composite microspheres with well-designed nanostructure: a highly integrated catalyst system, J. Am. Chem. Soc. 132 (2010) 8466–8473.
[18] S.H. Joo, J.Y. Park, C.K. Tsung, Y. Yamada, P. Yang, G.A. Somorjai, Thermally stable Pt/mesoporous silica core–shell nanocatalysts for high-temperature reactions, Nat. Mater. 8 (2009) 126.
[19] S.K. Kang, R.K. Murphy, S.W. Hwang, S.M. Lee, D.V. Harburg, N.A. Krueger, J. Shin, P. Gamble, H. Cheng, S. Yu, Bioresorbable silicon electronic sensors for the brain, Nature 530 (2016) 71.
[20] C.C. Liu, W. Feng, Y. Yao, Quantum spin Hall effect in silicene and two-dimensional germanium, Phys. Rev. Lett. 107 (2011), 076802.
[21] X. Wang, Z. Wu, Comment on "d+ i d′ chiral superconductivity in bilayer silicene", Phys. Rev. Lett. 114 (2015), 099701.
[22] C. Xu, G. Luo, Q. Liu, J. Zheng, Z. Zhang, S. Nagase, Z. Gao, J. Lu, Giant magnetoresistance in silicene nanoribbons, Nanoscale 4 (2012) 3111–3117.
[23] H. Lin, S. Gao, C. Dai, Y. Chen, J. Shi, A two-dimensional biodegradable niobium carbide (MXene) for photothermal tumor eradication in NIR-I and NIR-II biowindows, J. Am. Chem. Soc. 139 (2017) 16235–16247.
[24] D. Chiappe, C. Grazianetti, G. Tallarida, M. Fanciulli, A. Molle, Local electronic properties of corrugated silicene phases, Adv. Mater. 24 (2012) 5088–5093.
[25] Z. Guo, Y. Zhang, H. Xiang, X. Gong, A. Oshiyama, Structural evolution and optoelectronic applications of multilayer silicene, Phys. Rev. B 92 (2015), 201413.
[26] L. Wang, Y. Li, L. Zhao, Z. Qi, J. Gou, S. Zhang, J. Zhang, Recent advances in ultrathin two-dimensional materials and biomedical applications for reactive oxygen species generation and scavenging, Nanoscale 12 (2020) 19516–19535.
[27] Z. Gu, S. Zhu, L. Yan, F. Zhao, Y. Zhao, Graphene-based smart platforms for combined cancer therapy, Adv. Mater. 31 (2019), e1800662.
[28] N. Kong, X. Ji, J. Wang, X. Sun, G. Chen, T. Fan, W. Liang, H. Zhang, A. Xie, O. Farokhzad, W. Tao, ROS-mediated selective killing effect of black phosphorus: mechanistic understanding and its guidance for safe biomedical applications, Nano Lett. 20 (2020) 3943–3955.
[29] W. Tao, N. Kong, X. Ji, Y. Zhang, A. Sharma, O. Jiang, B. Qi, J. Wang, N. Xie, C. Kang, H. Zhang, O.C. Farokhzad, J.S. Kim, Emerging two-dimensional monoelemental materials (Xenes) for biomedical applications, Chem. Soc. Rev. 48 (2019) 2891–2912.
[30] L. Ma, X. Song, Y. Yu, Y. Chen, Two-dimensional silicene/silicon nanosheets: an emerging silicon-composed nanostructure in biomedicine, Adv. Mater. 33 (2021), e2008226.
[31] J. Liu, Y. Yang, P. Lyu, P. Nachtigall, Y. Xu, Few-layer silicene nanosheets with superior lithium-storage properties, Adv. Mater. 30 (2018), e1800838.
[32] E. Cinquanta, E. Scalise, D. Chiappe, C. Grazianetti, B. van den Broek, M. Houssa, M. Fanciulli, A. Molle, Getting through the nature of silicene: an sp2–sp3 two-dimensional silicon nanosheet, J. Phys. Chem. C 117 (2013) 16719–16724.
[33] L. Tao, E. Cinquanta, D. Chiappe, C. Grazianetti, M. Fanciulli, M. Dubey, A. Molle, D. Akinwande, Silicene field-effect transistors operating at room temperature, Nat. Nanotechnol. 10 (2015) 227.
[34] R.W. Redmond, J.N. Gamlin, A compilation of singlet oxygen yields from biologically relevant molecules, Photochem. Photobiol. 70 (1999) 391–475.
[35] P.C. Brooks, R.A. Clark, D.A. Cheresh, Requirement of vascular integrin alpha v beta 3 for angiogenesis, Science 264 (1994) 569–571.
[36] D.R. Green, J.C. Reed, Mitochondria and apoptosis, Sci 281 (1998) 1309–1312.
[37] M. Giorgio, E. Migliaccio, F. Orsini, D. Paolucci, M. Moroni, C. Contursi, G. Pelliccia, L. Luzi, S. Minucci, M. Marcaccio, Electron transfer between cytochrome c and p66Shc generates reactive oxygen species that trigger mitochondrial apoptosis, Cell 122 (2005) 221–233.
[38] N.N. Danial, S.J. Korsmeyer, Cell death: critical control points, Cell 116 (2004) 205–219.
[39] Y. Liu, X. Zhang, M. Zhou, X. Nan, X. Chen, X. Zhang, Mitochondrial-targeting lonidamine-doxorubicin nanoparticles for synergistic chemotherapy to conquer drug resistance, ACS Appl. Mater. Interfaces 9 (2017) 43498–43507.
[40] P.M. Rappold, M. Cui, J.C. Grima, R.Z. Fan, K.L. de Mesy-Bentley, L. Chen, X. Zhuang, W.J. Bowers, K. Tieu, Drp1 inhibition attenuates neurotoxicity and dopamine release deficits in vivo, Nat. Commun. 5 (2014) 5244.

[41] A.S. Moore, Y.C. Wong, C.L. Simpson, E.L. Holzbaur, Dynamic actin cycling through mitochondrial subpopulations locally regulates the fission–fusion balance within mitochondrial networks, Nat. Commun. 7 (2016), 12886.
[42] M. Karbowski, D. Arnoult, H. Chen, D.C. Chan, C.L. Smith, R.J. Youle, Quantitation of mitochondrial dynamics by photolabeling of individual organelles shows that mitochondrial fusion is blocked during the Bax activation phase of apoptosis, J. Cell Biol. 164 (2004) 493–499.
[43] L.V. Wang, S. Hu, Photoacoustic tomography: in vivo imaging from organelles to organs, Sci 335 (2012) 1458–1462.